



A novel full-process test bench for deep-sea in-situ power generation systems



Dayu Zhang ^{a,1}, Kaixin Chai ^{b,1}, Penghua Guo ^{a,*}, Qiao Hu ^c, Jingyin Li ^a, Ayesha Shams ^a

^a School of Energy and Power Engineering, Xi'an Jiaotong University, Xi'an, PR China

^b Institute of Artificial Intelligence and Robotics, Xi'an Jiaotong University, Xi'an PR China

^c School of Mechanical Engineering, Xi'an Jiaotong University, Xi'an, PR China

ARTICLE INFO

Handling editor: G Iglesias

Keywords:

Test bench

Hydrokinetic turbine model

In-situ power generation

Deep sea

Hydrokinetic energy conversion systems

ABSTRACT

A novel full-process test bench was developed to replace lengthy and costly deep-water experiments. This platform can accurately simulate the dynamic characteristics of hydrokinetic turbines and can be used to evaluate their power-supply capabilities under various conditions. The hydrokinetic turbine power model was established by obtaining discrete performance data through experimentally validated computational fluid dynamics simulations and building surrogate models using the response surface methodology. This approach offers higher accuracy and broader applicability than empirical models. Moreover, a stepper motor platform based on a speed control scheme is proposed for the first time that can achieve high-precision transient simulation with a simplified control mechanism. This platform was employed to assess the power supply capacity of two hydrokinetic turbines under constant and typical deep-sea flow speeds. The ductless Archimedes screw hydrokinetic turbine was found to be more suitable for the deep water application than the high-solidity horizontal axis turbine due to its high self-start capacity and power coefficient. Furthermore, a case study was conducted on the design of a deep-sea in-situ power generation system at Luzon Undercurrent. Results suggest that a ductless Archimedes screw hydrokinetic turbine with a 1000 mm radius can comfortably cater to the energy demands of miniature AUVs.

1. Introduction

Expanding the deployment range of deep-sea observation equipment is a prerequisite for exploiting the rich mineral and biological resources of the deep sea [1]. However, the issue of power supply remains a significant bottleneck for deep-sea observation equipment, limiting their long-term operation and deployment range [2]. Established technologies for powering sensors include research vessels [3] and cable nodes [4]. Utilizing research vessels, such as those involved in the Global Ocean Ship-based Hydrographic Investigations Program, will incur substantial costs, surpassing hundreds of thousands of dollars in daily maintenance expenses [5]. Although utilizing cable nodes for sensor installation can be more economical compared to research vessels, it necessitates the construction of infrastructure including fiber optic cables, subsea terminals, and secondary junction boxes [6], which not only has a substantial ecological impact on the oceans but also presents considerable challenges in maintenance.

Our previous research presented an innovative concept of a deep-sea in-situ power generation system [7,8]. This system could potentially supply power to cable-free undersea observatories, extending the range and adaptability of sensor deployment by harnessing deep ocean current energy [9]. Nonetheless, deep-sea in-situ power generation system is still an emerging technology, requiring extensive, long-term experimentation to ascertain essential performance parameters, such as power supply capacity. These parameters form the foundation for equipment design and are crucial for enhancing the system's reliability and performance.

The in-field validation experiment in deep water is generally time-consuming and cost-intensive, requiring a research vessel to be moored for an extended period [10]. The deep-water experiments can cost approximately \$200,000 or more per experiment and are heavily dependent on favorable weather conditions [11]. A possible way to speed up the development process and reduce experimental expenses is to use test benches in the laboratory instead of conducting in-field experiments. Such a platform can control motors through various control

* Corresponding author.

E-mail address: penghuagu@mail.xjtu.edu.cn (P. Guo).

¹ Indicates equal contribution.

Nomenclature

C_p	Power coefficient
c_{in}	Inner chord length (mm)
c_{out}	Outer chord length (mm)
D	Turbine diameter (mm)
D_{in}	Inner diameter (mm)
i	Rotation rate
J	Moment of inertia (kg m^2)
L	Turbine length (mm)
k	Blade curvature (m^{-1})
n	Number of turn
p	Screw pitch (mm)
R	Rotor radius (mm)
T	Torque (N m)
V	Velocity (m s^{-1})
<i>Greek symbols</i>	
α	Blade inclination with respect to axle ($^\circ$)
θ	Lead angle
ρ	Water density (kg m^{-3})
ω	Rotational speed (rad s^{-1})

algorithms to replicate the dynamic characteristics of turbines. By integrating appropriate generators and power supply systems, it can output the real-time electrical power of the deep-water in-situ power generation system under different conditions.

However, no test bench have yet been reported for ocean current energy utilization. Similar motor platforms have been utilized in the wind energy industry to assess the performance of wind turbines. Large grid-connected wind turbines are significantly affected by structural deformations and system vibrations [12,13]. Hence, torque control schemes, which govern motors to generate torque identical to turbines, are commonly used to simulate instantaneous dynamic characteristics [14]. For instance, Averous et al. [15] established a full-size megawatt-level wind-turbine test bench that simulated the forces experienced by a wind turbine under 6°-of-freedom stress, thereby obtaining operational data under extreme conditions. This approach necessitates considering the difference in rotational inertia between the motor and the turbine, typically addressed by adding extra flywheels or employing electric inertia compensation methods to offset the inertia difference [16]. However, adding extra flywheels complicates the mechanical design, while utilizing electric inertia compensation methods can introduce noise in the feedback speed, leading to incorrect compensation and system instability. Li et al. [17] conducted a theoretical analysis to explore the instability arising from the inertia emulation scheme and quantified the conditions necessary to maintain system stability. Several research groups have proposed additional control methods to mitigate torque fluctuations and errors, for example, the use of discrete space vector modulation to reduce torque fluctuations at low rotational speeds [18].

Contrary to large grid-connected wind turbines, deep-sea hydrokinetic turbines are relatively smaller devices, where the elastic deformation induced by forces and torques across other degrees of freedom can be disregarded. Hence, this study proposes a more stable speed control scheme to simulate the instantaneous dynamic characteristics of hydrokinetic turbines. Given that in the speed control scheme, the motor's rotational speed is directly determined based on the generator load torque and turbine power characteristics from the previous moment, this control strategy can avoid torque oscillation in the dynamic process [19]. Another distinction between deep-sea hydrokinetic turbines and large wind turbines manifests in the power model. Large wind turbines have a converged technological pathway, predominantly adopting

three-blade lift-type turbines, which share similar maximum C_p and optimal tip speed ratio (TSR). This allows for the utilization of empirical models [20] or theoretical models, such as the blade element momentum (BEM) theory [21], to obtain turbine dynamic characteristics.

In contrast, deep-sea hydrokinetic turbines represent an emerging technology with an unconsolidated technological pathway. Various novel hydrokinetic turbines, including high-solidity horizontal axis turbines (HSHAT) [9] and ductless Archimedes screw turbines (DAST) [7], hold potential as power modules in deep-sea in-situ power generation systems due to their excellent self-starting capabilities. These hydrokinetic turbines vary significantly in terms of maximum C_p and optimal TSR and lack reliable empirical or theoretical models for reference. Moreover, given that deep ocean currents are substantially slower than shallow ocean currents, researchers are more concerned with the start-up ability and the transient start-up characteristics of turbines under different deep ocean current conditions. Existing empirical and theoretical models fall short in addressing transient issues during the start-up process.

To address such issues, this paper introduces a CFD-surrogate model approach, leveraging CFD software to acquire discrete power data and employing response surface methodology to establish turbine power models. This approach is capable of accurately simulating the dynamic characteristics of various novel hydrokinetic turbines under various operating conditions, including a more precise replication of transient startup characteristics.

Based on the proposed speed control scheme and the CFD-surrogate model approach, a full-process test bench for deep-sea in-situ power generation systems was developed in the present study. This test bench can test the power supply and startup capabilities of all types of deep-sea hydrokinetic turbines under various deep-sea conditions. The simulation results can serve as a valuable reference for practical applications, or as a component of the optimization process, where adjustments to the design parameters of the hydrokinetic turbines and the power supply system can be made to further enhance the power generation system's capacity.

2. Description of the full-process test bench

Fig. 1 depicts the establishment process of the proposed full-process simulation. The schematic of the subject of this study, the deep-sea in-situ power generation system, is illustrated in Fig. 1 (a). The objective of this power generation system is to harness deep ocean current energy to supply power to cable-free undersea observatories, thereby extending the range and adaptability of deep-sea sensor deployment.

Fig. 1 (b) shows the in-field validation experiment process for testing this power system, a procedure necessitating the deployment of the system into the deep sea. This process is both time-consuming and financially demanding, requiring the secondary retrieval of equipment for data collection. Conversely, Fig. 1 (c) illustrates the utilization of test benches in a laboratory setting. This strategy markedly accelerates the developmental pace of the deep-sea in-situ power generation system while curbing experimental costs. The cornerstone of creating such a platform is developing a power model, which, when coupled with control algorithms, enables the motor to replicate the dynamic characteristics of turbines accurately.

As illustrated in Fig. 1 (d), this paper introduces a CFD-surrogate model approach for crafting the power model. Initially, CFD simulations were employed as a sampling method to compute the dynamic characteristics of the hydrokinetic turbine across various rotational and current speeds. The Design of Experiment (DoE) methodology was utilized to determine the positions of the sampling points. The goal of this DoE is to ensure that the sampling points uniformly cover the turbine's operational range, thereby enabling the identification of the optimal combination of factor levels. These CFD simulation outputs then served as inputs for a fitting method, facilitating the construction of surrogate models for dynamic characteristics. Given the number of independent variables in the power model, a full factorial experimental design was

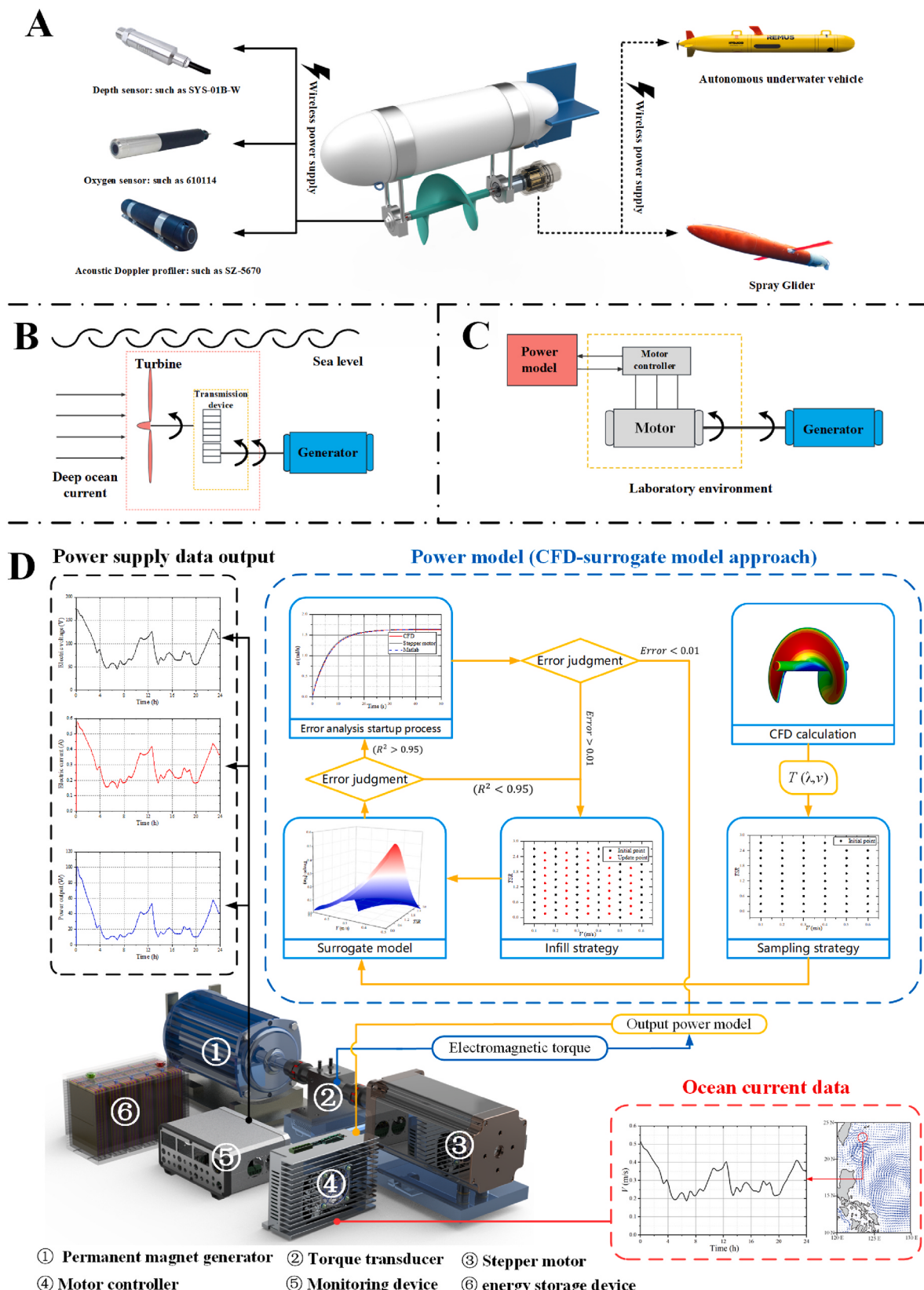


Fig. 1. Establishment process of the full-process test bench.

employed for the DoE approach and used Response Surface Methodology (RSM) for the fitting process. The primary advantage of the CFD-surrogate model over direct CFD simulation lies in its significant reduction of computational time needed to assess the dynamic characteristics of the hydrokinetic turbine. This efficiency enables the full-process test bench to achieve transient simulation capabilities.

The R-squared (R^2), adjusted R-squared ($AdjR^2$), and predicted R-squared ($PredR^2$) of the surrogate model were regarded as criteria to evaluate the goodness-of-fit of the surrogate model. They are defined as follows:

$$R^2 = 1 - \left[\frac{SS_{\text{residual}}}{(SS_{\text{residual}} + SS_{\text{model}})} \right] \quad (1)$$

$$AdjR^2 = 1 - \left[\frac{\left(\frac{SS_{\text{residual}}}{DF_{\text{residual}}} \right)}{\left(\frac{SS_{\text{residual}} + SS_{\text{model}}}{DF_{\text{residual}} + DF_{\text{model}}} \right)} \right] \quad (2)$$

$$PredR^2 = 1 - \left[\frac{PRESS}{SS_{\text{residual}} + SS_{\text{model}}} \right] \quad (3)$$

$$SS_{\text{residual}} = \sum_{i=1}^n (y_i - f(x_i))^2 \quad (4)$$

$$SS_{\text{model}} = \sum_{i=1}^n f(x_i)^2 \quad (5)$$

$$PRESS = \sum_{i=1}^n (y_i - \hat{y}_{i,-i})^2 \quad (6)$$

Where SS_{residual} is the sum of the squares of residuals and SS_{model} is the sum of the squares of models. DF_{residual} and DF_{model} are the degrees of freedom of residual and surrogate model. $PRESS$ is predicted residual error sum of squares. If any of these values are less than 0.95, an infill strategy will be conducted to enhance the performance of the surrogate model.

Upon meeting the requisite goodness-of-fit standards, an error analysis is undertaken. This involves juxtaposing the real-time rotational speed curve acquired during the startup process via the motor platform against the numerical outcomes derived from a CFD simulation utilizing a six-degree of freedom model. This comparison aims to quantify deviations stemming from transient characteristics in the flow field, truncation errors, and mechanical transmission. Following the acquisition of ocean current data and generator load torque measured by torque sensors, the motor controller leverages the speed control scheme to directly determine the motor's rotational speed for the next moment. Through the transmission device, the motor supplies torque to a permanent magnet generator, with the resultant electrical energy being transmuted into chemical energy within the energy storage system via a charging controller. Throughout this operation, instruments record and output the real-time power supply status.

The full-process test bench can not only obtain the steady-state power supply capacity of the power generation system under constant current speed but also provide long-term operational data and power supply capabilities under actual ocean current conditions. It can serve as a valuable design reference for practical applications and facilitate optimizing the MPPT control and power supply strategies. Furthermore, the long-term operational data can be utilized as a learning sample for neural network-based control strategies, enabling further optimization of turbine performance, MPPT control strategy, and charge controllers.

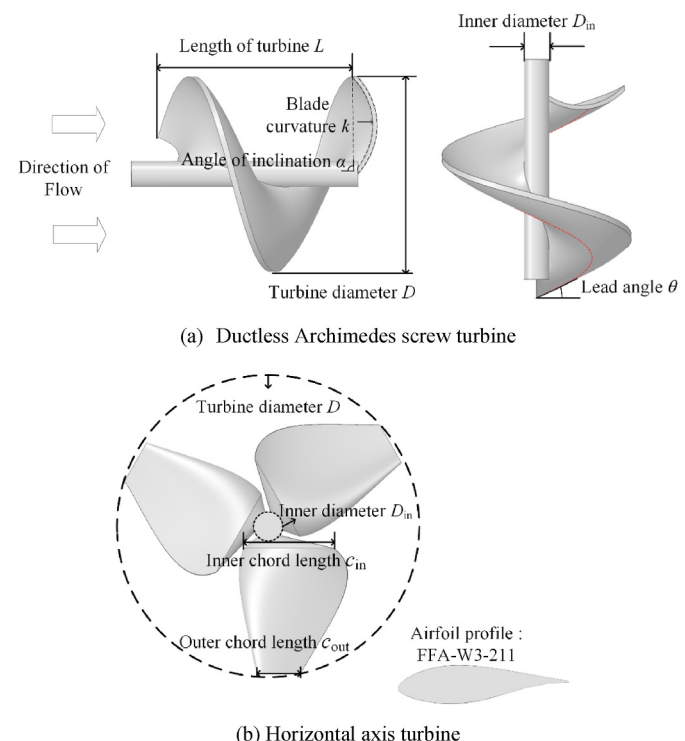


Fig. 2. Geometrical parameters of turbines.

Table 1
Geometrical parameters of the DAST.

	D (mm)	α (°)	n	θ (°)	k (m^{-1})	L (mm)	D_{in} (mm)
DAST	1000	90.21	1.25	34.10	8.06	1000	133

Table 2
Geometrical parameters of the HSHAT.

	D (mm)	c_{in} (mm)	c_{out} (mm)	Airfoil	D_{in} (mm)
HAHT	1000	174	70	FFA-W3-211	133

3. CFD simulation

The torque characteristics of hydrokinetic turbines were analyzed utilizing the commercial CFD software Ansys Fluent 2020 R2. DASTs and HSHAT were chosen as research objects due to their excellent self-starting performance in low current-speed environments. The evaluation of DAST and HSHAT's performance was carried out through the metrics of power coefficient C_p and tip speed ratio (TSR), defined by the following equations:

$$C_p = \frac{T\omega}{0.5\rho\pi R^2 V^3} \quad (7)$$

$$TSR = \frac{\omega R}{V} \quad (8)$$

where T stands for the torque (Nm), ω represents the rotational speed (rad s^{-1}), ρ denotes the water density (kg m^{-3}), R is the rotor radius (m), and V indicates the flow speed (m s^{-1}).

3.1. Turbine rotor geometry

The geometric parameters of the DAST and HSHAT are shown in Fig. 2 and Tables 1 and 2. The geometric parameters of the DAST were

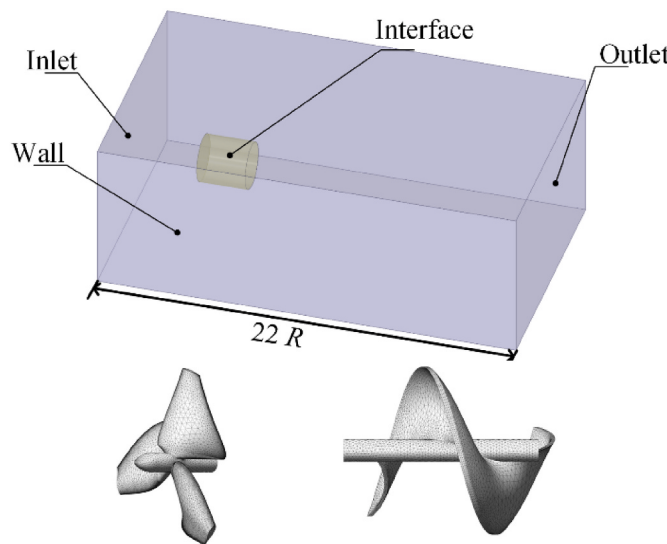


Fig. 3. Computational domain and grids.

derived from our previous study of multi-objective optimization for efficiency and self-starting ability [7]. The airfoil of HSHAT was selected to FFA-W3-211, and the design method is the Wilson design method with a design TSR of 2.

3.2. Simulation setup

The sliding mesh approach was employed to facilitate the transient rotation of the turbine. The computational domain consists of a fixed and rotating subdomain, which were discretized using unstructured tetrahedral and structured hexahedral meshes, as shown in Fig. 3. The tested sectional area of the domain was 500 times larger than the turbine cross-sectional area, with the rotating subdomain centrally positioned in the cross-section. The grid independence test revealed a maximum C_p deviation of no more than 0.5 % with over 3 million nodes. The simulation adopted a time step size equating to a 1° rotation of the turbine. The C_p value was derived from the average of the final four cycles in a series of eight complete turbine revolutions. Additionally, the torque T in the static case was averaged from 20 to 40 s.

The study utilized the Reynolds-averaged governing equations to analyze turbulent flows characterized by unsteadiness, three-dimensionality, and incompressibility. The chosen turbulence model for this study was the shear stress transport (SST) $k-\omega$. The pressure, momentum, and turbulence equations were solved using the SIMPLE

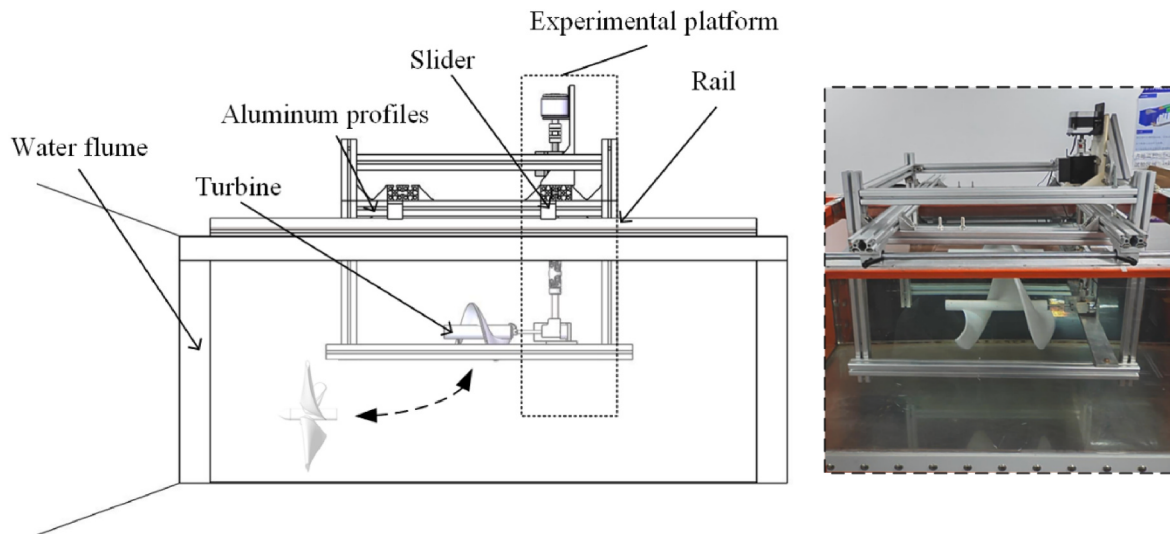


Fig. 4. Sketch of experimental apparatus for the DAST and the horizontal axis turbine.

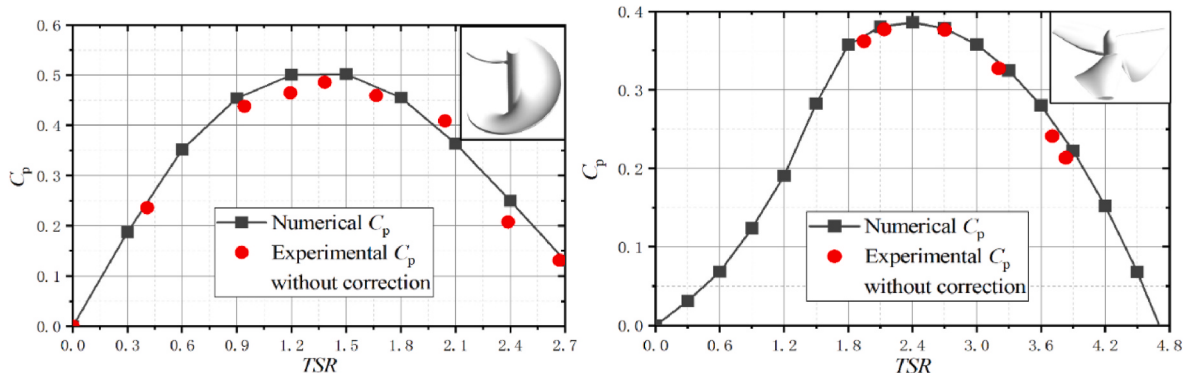


Fig. 5. Validation of C_p between experiment and simulation.

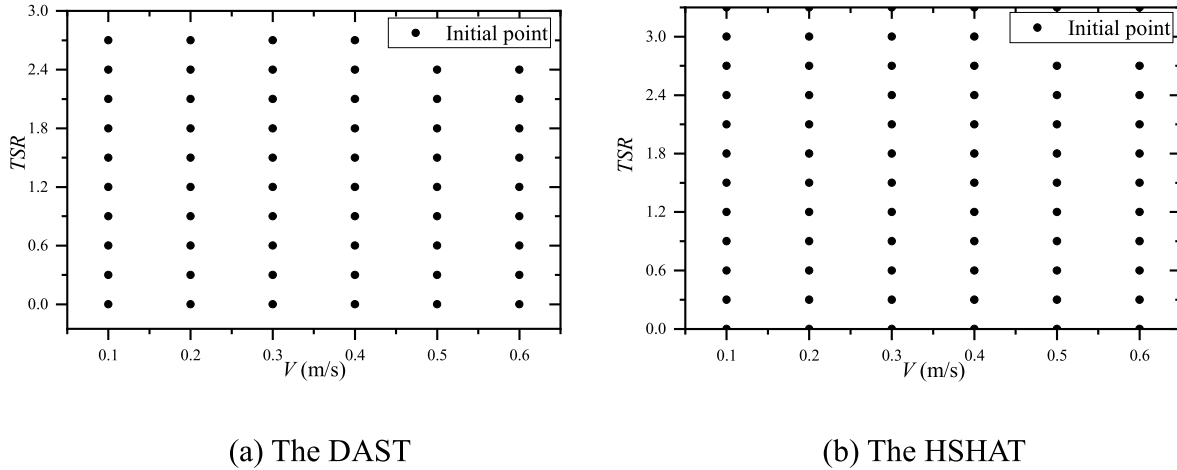


Fig. 6. Sampling points of the DAST and the HSHAT.

algorithm coupled with a second-order upwind spatial discretization scheme. To satisfy the prerequisites of the (SST) $k-\omega$ turbulence model, a y^+ value of 1 was targeted. The simulations were executed with a stringent absolute convergence criterion set at 10^{-5} for various parameters, including continuity, velocity components, and turbulence attributes.

3.3. Validation of the numerical method

To validate the accuracy of the numerical method, a water flume experiment was conducted. Due to the limited size of the test section, scaled-down hydrokinetic turbines were used instead of full-scale ones. These scaled-down models had a diameter and height of 300 mm. The experimental setup consisted of a circulating water flume with a test section measuring 1000 mm in length, 500 mm in height, and 800 mm in width, as illustrated in Fig. 4. Torque and rotational speed measurements were obtained using a torque transducer connected to a magnetic powder brake, with a maximum capacity of 10 Nm. Mechanical friction, which resulted from components like bearing seats, coupling, commutator, and cardan joint, was measured to be below 0.03 Nm using the balance method.

The test turbines used in these experiments were fabricated using

polylactic acid through 3D printing. These turbines were positioned 500 mm downstream of the test section entrance. To evaluate the turbine's performance under low-speed conditions, the experimental current speed was set to 0.5 m/s, which is typical for deep sea.

Fig. 5 presents a comparison between the experimental data and simulation results. It is evident that the simulation results closely align with the experimental data. The maximum relative error observed is less than 5 %, signifying that the numerical method employed in this study is capable of predicting results with a high degree of accuracy.

The hydrodynamic differences between the HSHAT and the DAST are primarily due to the significant axial length of the DASTs [22]. It causes less blockage effect at the same solidity, allowing a greater flow velocity to pass through compared to the HSHAT. Blades of the HSHAT located on the same plane, resulting in a more pronounced blockage effect and consequently, more flow bypassing the turbine. This difference is instrumental in enhancing the DASTs' power coefficient slightly above that of HSHATs. Furthermore, the solidity of DASTs exceeds 1, enabling them to utilize the entire flow within cross-sectional area of turbines in static state. HSHATs cannot exploit the gaps between blades in the same condition. Coupled with DASTs' greater twist angle, their static torque coefficient substantially exceeds that of HSHATs, with their peak power coefficient corresponding to a lower TSR compared to HSHATs.

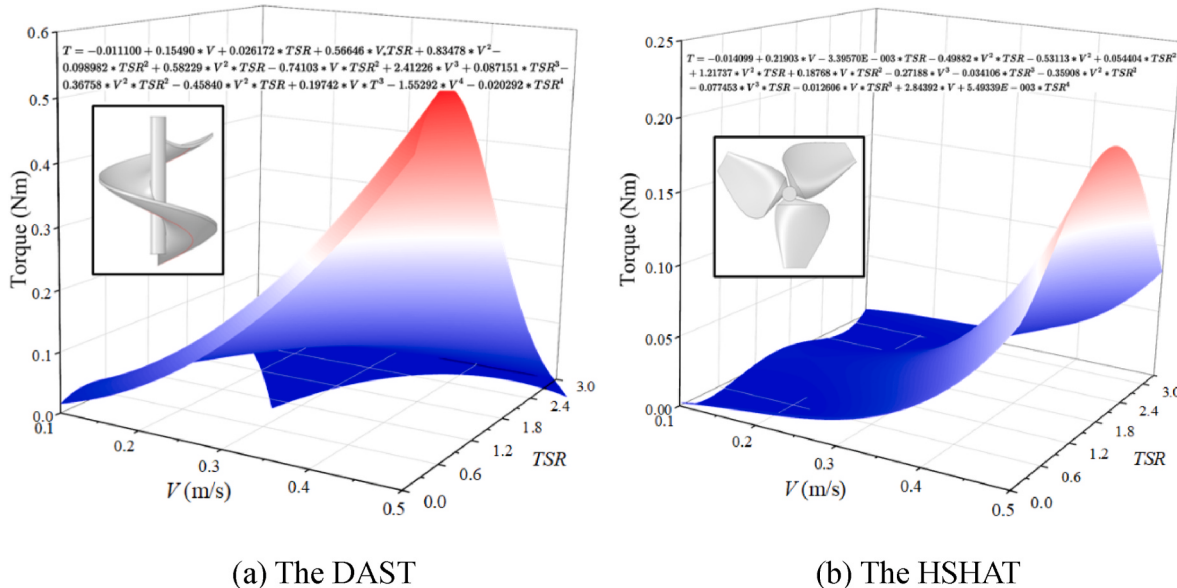


Fig. 7. Torque surrogate model of hydrokinetic turbines.

Table 3

Judgement standard of the surrogate models.

	R^2	$AdjR^2$	$PredR^2$
DAST	0.994	0.995	0.984
HSHAT	0.991	0.989	0.978

4. Experimental design and surrogate model

The full factorial experimental design was adopted in this section, with the independent variables being the current speed V and TSR , while the dependent variable was the torque. The sampling schemes are shown in Fig. 6. Fourth-order response surface models for the T were obtained by performing a least squares fit, as shown in Fig. 7.

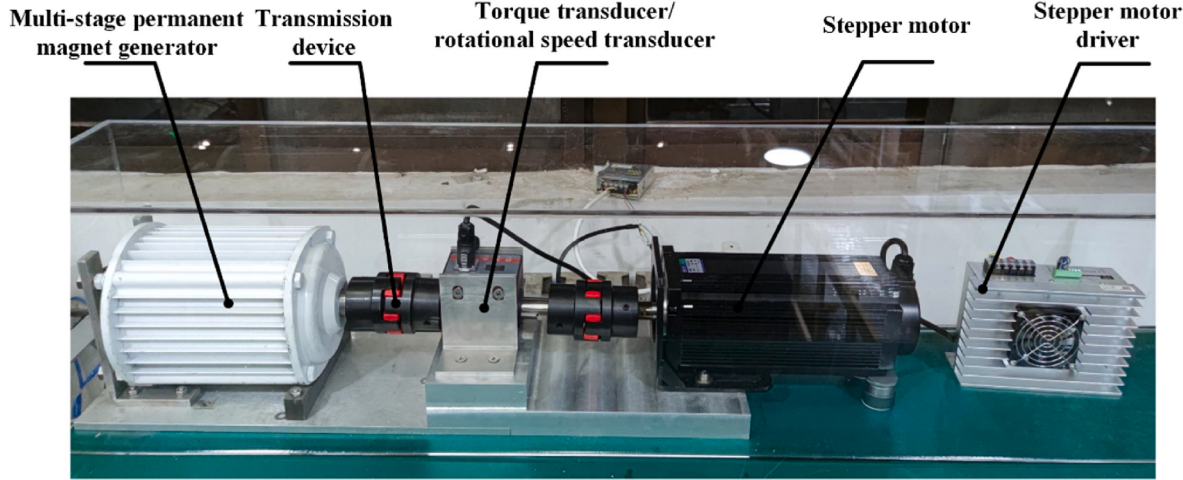


Fig. 8. Diagram of stepper motor test bench.

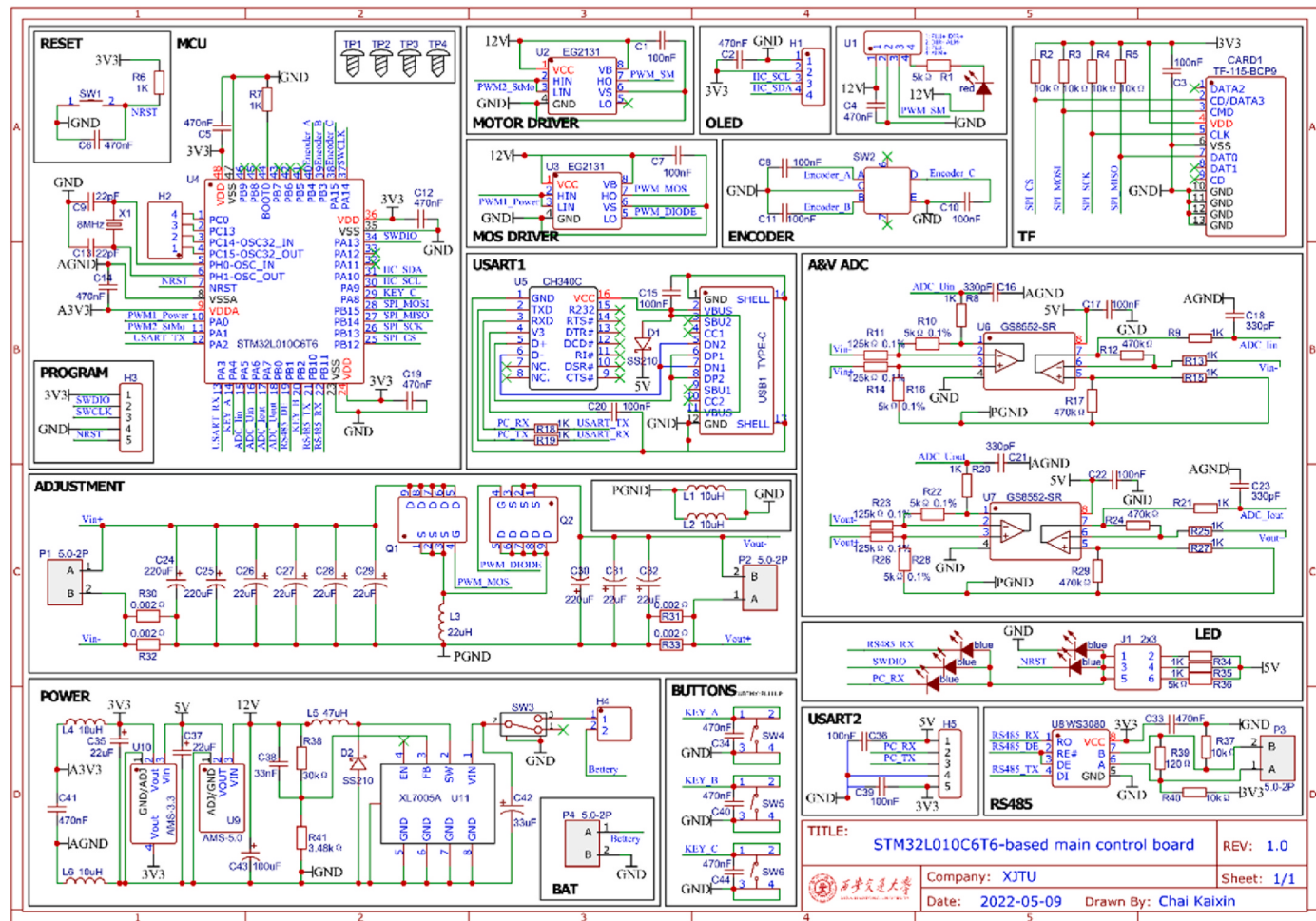


Fig. 9. Main control board circuit schematic.

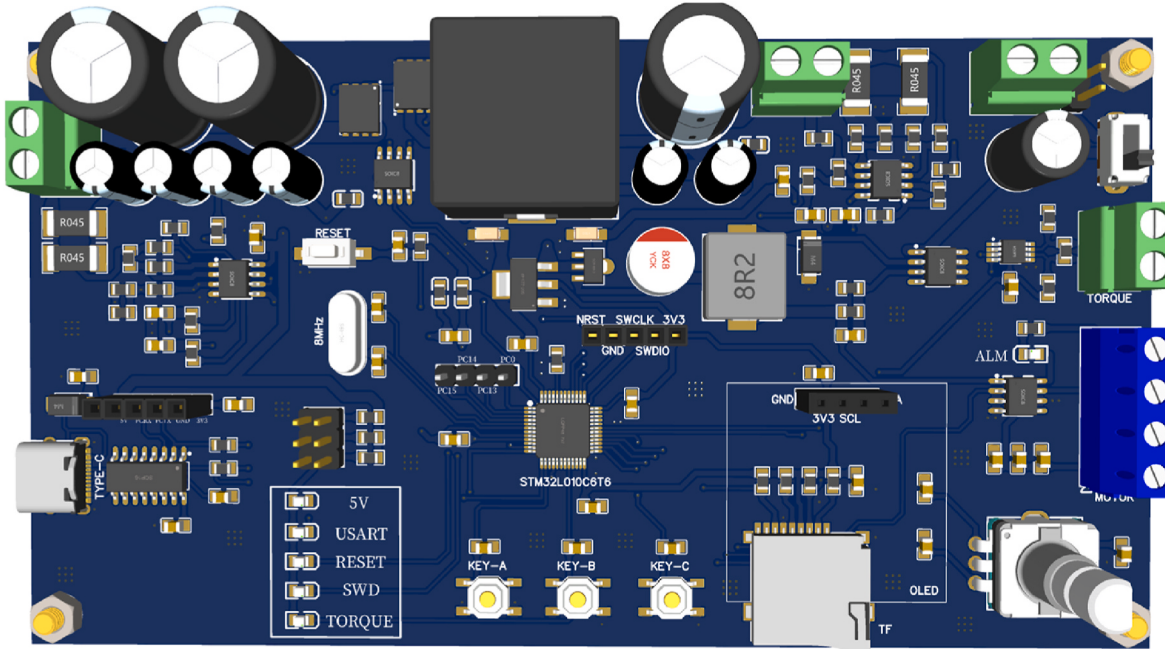


Fig. 10. Main control board 3D rendering.

The performance of the RSM can be assessed by considering the R^2 , adjusted R -squared $AdjR^2$, and predicted R -squared $PredR^2$ together, as listed in Table 3. The coefficient of determination R^2 is used to evaluate the goodness-of-fit of the model. The higher the value of R^2 , the better the model fits the data. The torque surrogate models the DAST and the HSHAT show $R^2 = 0.994$ and $R^2 = 0.991$, respectively, which demonstrate that only 0.006 and 0.009 of the total variations are not explained. At the same time, since R^2 always increases as data points are added to the model, it is necessary to use the adjusted coefficient of determination $AdjR^2$, which is always smaller than R^2 and decreases with the addition of points, to penalize R^2 . The values of $AdjR^2$ (0.995 and 0.989, respectively), are extremely close to the corresponding R^2 , which indicates that the data points and values of R^2 are highly reasonable. The high values of the predicted coefficients of determination $PredR^2$ (0.984 and 0.978, respectively), which represent how well the model predicts responses for new observations, also illustrate great

performance of the models. Therefore, the results obtained in this work indicate that the surrogate models can ensure a satisfactory goodness of fit for the data and provide a reasonably accurate prediction.

5. Motor test bench

A novel stepper motor test bench was proposed for deep-water hydrokinetic turbines with the aim of providing a dynamic moment equivalent to that of an actual hydrokinetic turbine, as shown in Fig. 8. This equivalence is facilitated by a stepper motor controller executing a speed control strategy. Upon acquiring ocean current data and generator load torque as measured by torque sensors, the motor controller utilizes turbine power models established through the CFD-surrogate model approach to directly determine the motor's rotational speed for the subsequent moment. A microcontroller is used to implement the speed control strategy in this study. Detailed schematics of the main control board circuit and structural illustrations are shown in Figs. 9 and 10, respectively.

This strategy subtracted the load torque measured by the torque meter from the driving turbine torque produced by the hydrokinetic turbine to obtain the net torque and speed increment, thus obtaining the real-time speed. The dynamic equation of the speed control strategy is:

$$\left\{ \begin{array}{l} J : \text{Moment of inertia}(\text{low speed axis}) \\ J \frac{d\omega}{dt} = T - T_{ls} \quad T_{ls} : \text{Low speed braking torque} \\ J_h \frac{d\omega_g}{dt} = T_{hs} - T_f - T_{em} \quad J_g : \text{Moment of inertia}(\text{high speed axis}) \\ \omega_g : \text{Rotational speed}(\text{high speed axis}) \\ i = \frac{\omega_g}{\omega} \quad T_{hs} : \text{High speed dynamic torque} \\ i^2 = \frac{J}{J_h} \quad T_f : \text{Frictional torque} \\ T_{em} : \text{Electromagnetic torque} \\ i : \text{Rotation rate} \end{array} \right. \quad (9)$$

The Euler method was employed to discretize the time variable for calculating the rotational speed increment. Assuming the rotational speed at time t_n is represented as ω_n , and the torque difference is $T - T_{ls}$, then the rotational speed at time t_{n+1} can be determined as:

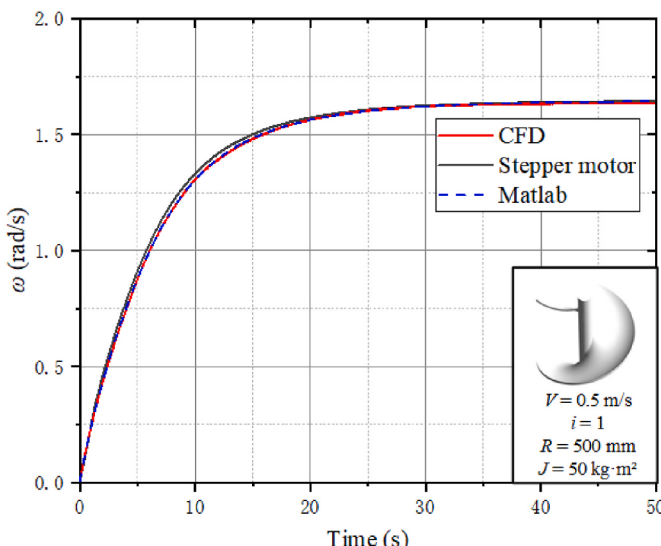


Fig. 11. Comparison of the dynamic characteristics from the motor platform, CFD and Matlab.

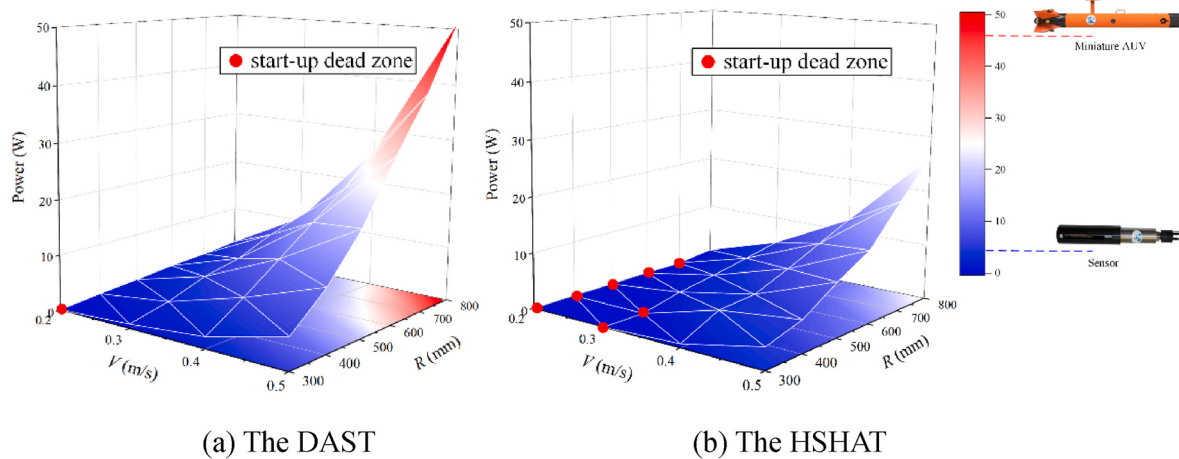


Fig. 12. Power output capacity of DAST and HSHAT under various turbine radius and flow speed.

$$\omega_{n+1} = \omega_n + \frac{1}{J} (T_{(n)} - T_{ls(n)}) \quad (10)$$

The dynamic characteristics of the stepper motor platform deviate from those of the actual hydrokinetic turbine in three ways. Firstly, the transient characteristics in the flow field of the actual hydrokinetic turbine, such as torque fluctuations caused by periodic vortex shedding, are disregarded. Secondly, the time discretization method and time step introduce truncation errors. Lastly, the deviation comes from the mechanical transmission.

To verify the accuracy of the stepper motor test bench and to quantify the deviation from the actual hydrokinetic turbine, the real-time rotational speed curve obtained by the motor platform was compared with numerical results from CFD simulation using a six-degree of freedom model and theoretical calculations using an ideal dynamic model by MATLAB. The dynamic characteristics produced by the six-degree of freedom model are devoid of the three sources of deviation mentioned above. Considering that hydrokinetic turbines are relatively smaller devices, the elastic deformation induced by forces and torques across other degrees of freedom can be disregarded. Therefore, only the rotational freedom around the axis is activated.

The ideal power model running in MATLAB can employ a minimal timestep, thus avoiding truncation errors caused by the time discretization method and time step. As shown in Fig. 11, the comparison results demonstrate that the deviation values of the stepper motor platform are 0.8 % and 0.2 % compared to the ideal dynamic model run in MATLAB and the six-degree of freedom model in CFD, respectively. This indicates that the truncation errors from the time discretization method and timestep account for a significant portion of the total error. The dynamic characteristics of the stepper motor test bench have adequate accuracy.

6. Estimation of power supply capacity

The full-process test bench has been proven to simulate the dynamic characteristics of hydrokinetic turbines accurately. In this section, this platform was employed to assess the power supply capacity of the turbines under constant and variable flow speed conditions.

6.1. Steady simulation

Fig. 12 shows the power supply capacity of various turbine sizes under constant flow speeds. DAST displays a higher self-starting capability, self-starting at a current speed of 0.3 m/s for a turbine radius of 300 mm, or 0.2 m/s for a turbine radius of 400 mm. This makes it suitable for small-sized deep-sea power generation systems. When the flow speed exceeds 0.5 m/s and the turbine radius exceeds 500 mm, the

power generation system can produce 5 W, sufficient for most sensors continuously. If the turbine radius is larger than 700 mm and the flow speed exceeds 0.5 m/s, the deep-sea power generation system based on DAST can support the most miniature AUVs.

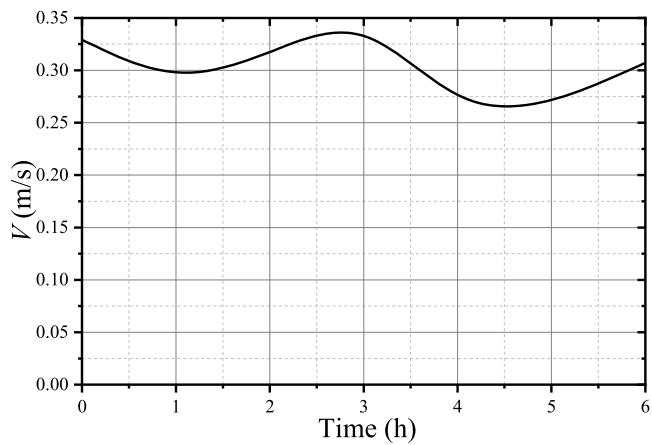
In contrast, HSHAT has a lower self-starting capability and requires a turbine radius of 800 mm at a current speed of 0.2 m/s to self-start. Moreover, under any working conditions, HSHAT's power supply capacity is less than half of DAST's. Therefore, even if the DAST is slightly heavier than the HSHAT, DAST remains more suitable for deep-sea power generation systems.

6.2. Transient simulation

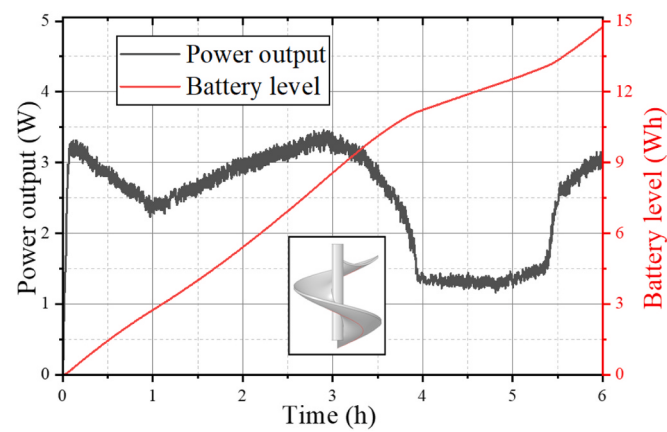
The steady-state simulation can only model the system's power supply under constant flow speed. It fails to simulate the turbine's start-up state and the system's power generation capability over a specified time interval under actual variable flow conditions. Therefore, in this section, the motor platform was utilized to assess the power generation capabilities of the HSHAT and the DAST, each with a radius of 500 mm, under actual variable flow conditions. Two typical ocean current data sets, with average speeds of 0.3 m/s and 0.7 m/s, respectively, each spanning a duration of 6 h, were input into the ocean current speed model.

As illustrated in Figs. 13 and 14, the results revealed that the DAST can start and stabilize in a relatively short timeframe. The time it takes for DAST to reach stable rotational speed is merely 25 % of what HSHAT requires. This suggests that DAST can capitalize on abrupt deep-sea currents more efficiently. However, the optimal TSR for HSHATs surpasses that of DASTs, resulting in the HSHATs achieving higher rotational speeds under identical flow conditions. If the generator has not yet reached the speed-efficiency threshold, the mechanical-to-electrical energy efficiency of HSHATs will marginally outperform DASTs. For example, during ultra-low flow speed conditions, between hours 4–5 (Fig. 13), the power output of both HSHATs and DASTs is virtually indistinguishable. However, as flow speeds escalate to a point where both turbines' speeds attain the speed-efficiency threshold, such as low flow speed conditions between hours 4–5 (Fig. 14), the power output from DASTs significantly surpasses that of HSHATs by more than 1.5 times.

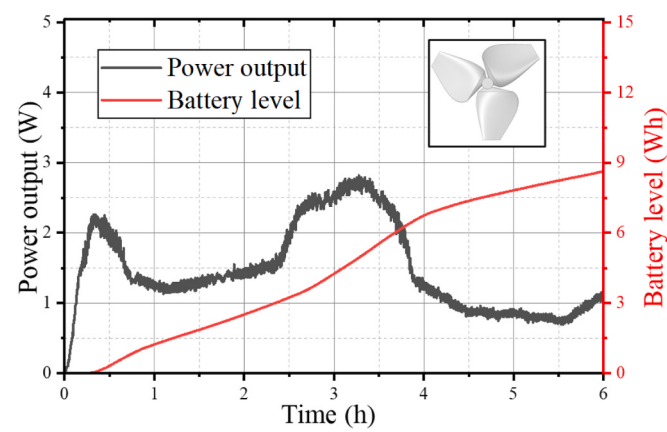
From a practical implementation standpoint, the solidity of DAST is twice that of HSHAT, making it heavier for a given cross-sectional area. However, as deep-water hydrokinetic turbines are considered small-scale mechanical devices, the augmented system weight neither introduces extra installation complications nor substantially elevates manufacturing costs. Hence, this study recommends DAST as a power apparatus for deep-water in-situ power generation systems.



(a) Ocean current data



(b) Real-time power supply data of DAST

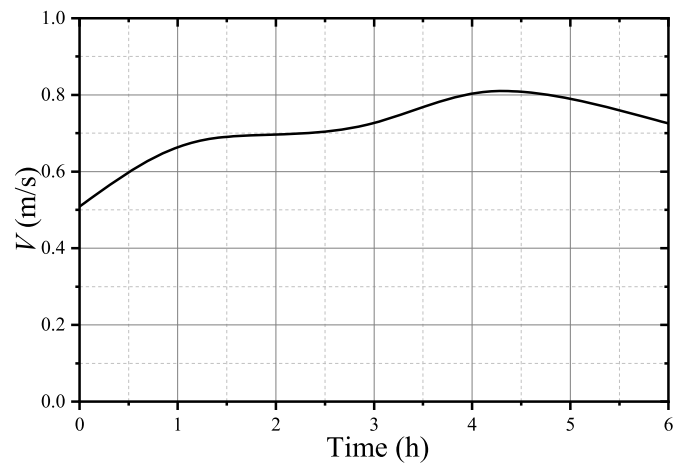


(c) Real-time power supply data of HSHAT

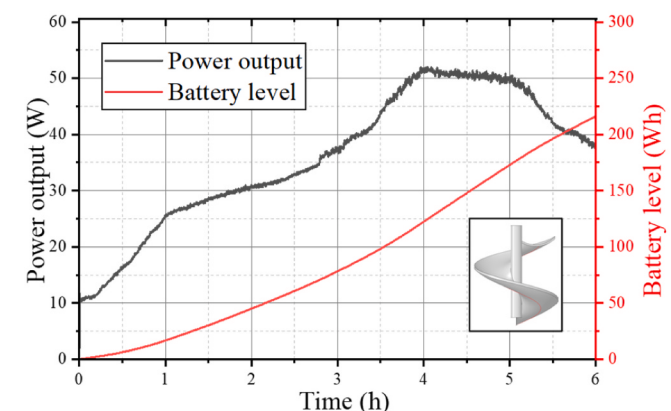
Fig. 13. Power output capacity of DAST and HSHAT under ultra-low flow speed conditions.

6.3. Case study for Luzon Undercurrent

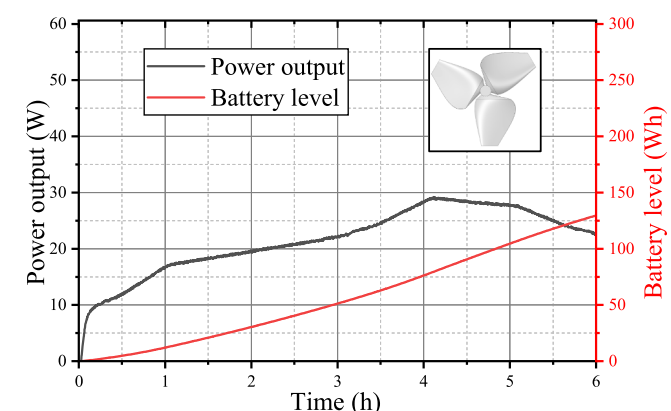
The Luzon Undercurrent is a subsurface current in the western tropical Pacific [23]. It plays a pivotal role in transporting subsurface and intermediate water masses, which are crucial for global thermohaline circulation and climate change [24]. Consequently, long-term hydrographic observations of the Luzon Undercurrent are of great



(a) Ocean current data



(b) Real-time power supply data of DAST

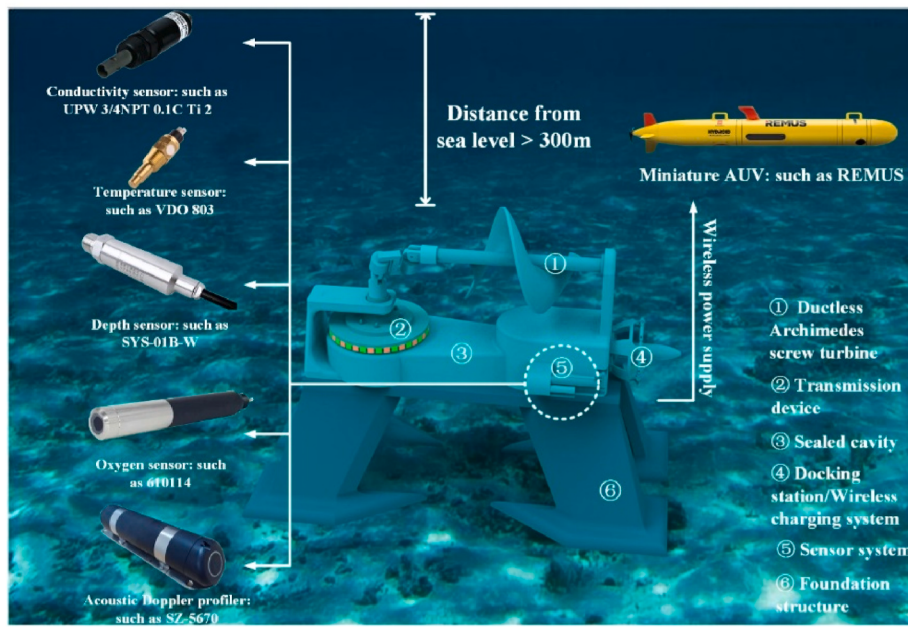


(c) Real-time power supply data of HSHAT

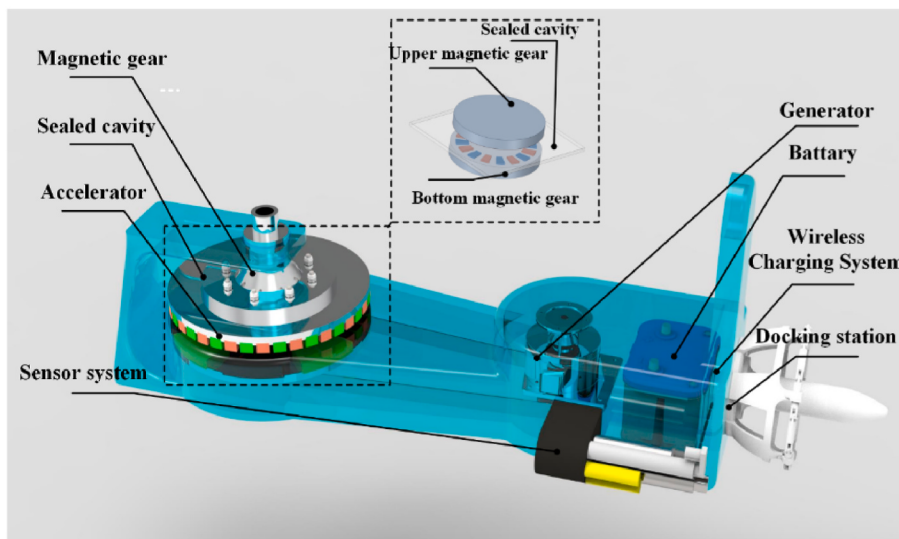
Fig. 14. Power output capacity of DAST and HSHAT under low flow speed conditions.

significance for the advancement of marine science. Cable-free undersea observatories can conduct long-term hydrographic observations without relying on ships or any fixed equipment for power supply (Fig. 15).

In this section, the proposed full-process test bench was used to determine the appropriate size of the DAST necessary to meet the energy demands of deep-sea exploration equipment. Given the distinct diurnal



(a) Application scenario



(b) Internal structure in the sealed cavity

Fig. 15. Schematic of the cable-free undersea observatory.

variation in the local ocean currents, 24-h ocean current data was loaded into the platform. An effective undersea observatory should feature various sensors, including conductivity-temperature-depth, oxygen, and an acoustic Doppler profiler, along with an AUV equipped with underwater cameras and other sensors. To ensure continuous operation of the sensors and AUV, which cruises once every 10 days, the daily energy requirement must exceed 200 Wh. Considering the seasonal and annual variations in local flow speed, the power supply system must have a certain degree of power redundancy.

As shown in Fig. 16, the location (24.403 N, 123.600E) with a depth of 300 m has a maximum flow speed of approximately 0.5 m/s, and a minimum flow speed close to 0.2 m/s. The daily power capacities of DASTs with the radius of 500 mm, 1000 mm, and 1500 mm are 45 Wh, 286 Wh, and 1020 Wh, respectively (Fig. 17). Based on these current

conditions, it is recommended to use a DAST with a radius of 1000 mm as the power supply unit for the in-situ power generation system to power multiple deep-sea exploration equipment. A DAST with a radius of 500 mm can provide power to a stationary deep-sea observation system without any propulsion equipment, but additional buoys or acoustic communication systems are required for hydrological information transmission. On the other hand, a DAST with a 1500 mm radius is capable of powering a medium-sized AUV, endowing it with a cruising range of 30 km and facilitating a cruise once every 20 days. Arrays designed with a deep-sea in-situ power generation system can efficiently power an AUV fleet, facilitating widespread and consistent deep-sea hydrographic surveillance.

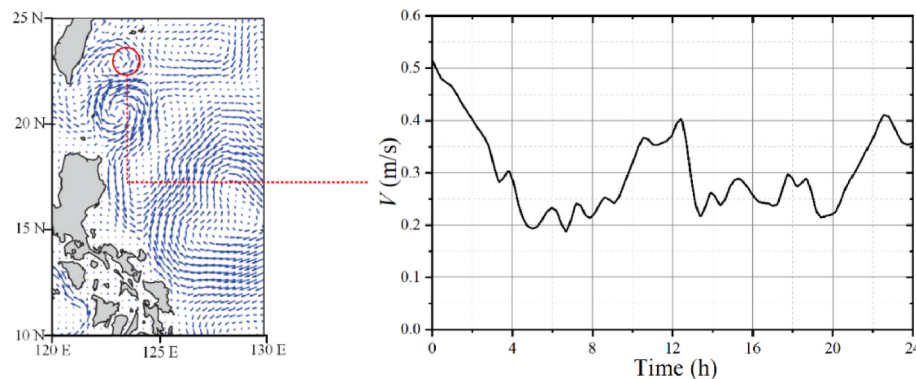


Fig. 16. Ocean current data of Luzon Undercurrent.

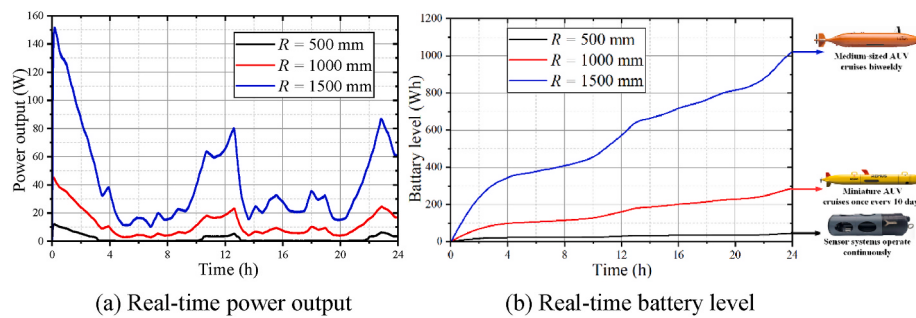


Fig. 17. Power supply data of DASTs of varying sizes.

7. Conclusion and future work

This paper presented a full-process test bench for deep-water in-situ power generation systems to replace expensive ocean testing experiments. A control strategy based on a validated hydrokinetic turbine torque surrogate model was developed and applied to a stepper motor to reproduce the turbine's hydrokinetic characteristics. The platform was used to evaluate the power supply capabilities of DAST and HSHAT in different flow environments and turbine sizes. The following conclusions are drawn.

- (1) The DAST's power output is 1.4 times greater than that of the HSHAT in deep water with low flow speed, making it a more suitable power unit for deep water in-situ power generation systems.
- (2) A 500 mm radius DAST power station can self-start in 0.2 m/s conditions, while it can produce over 12 Wh of power per day in conditions with an average flow rate of 0.3 m/s, sufficient to power continuously operating sensors. When the flow speed escalates to 0.7 m/s, the same-sized DAST can supply an impressive 800 Wh within a day, enough to sustain the operations of a miniature AUV.
- (3) The full-process test bench was used to forecast the power supply capacities for a deep-water in-situ power generation system projected for deployment in the Luzon Undercurrent. Results suggest that a DAST with a 1000 mm radius can comfortably cater to the energy demands of sensor systems and miniature AUVs.
- (4) In prospective applications, the full process test bench can be used to evaluate the effects of magnetic drive systems and different MPPT control strategies on deep-water in-situ power generation systems before ocean testing experiments.

CRediT authorship contribution statement

Dayu Zhang: Methodology, Writing – original draft, Conceptualization. **Kaixin Chai:** Software. **Penghua Guo:** Funding acquisition, Resources, Writing – review & editing. **Qiao Hu:** Resources. **Jingyin Li:** Supervision. **Ayesha Shams:** Validation.

Declaration of competing interest

The authors declare that they have no known competing financial interests or personal relationships that could have appeared to influence the work reported in this paper.

Acknowledgment

Data availability

Data will be made available on request.

This work was supported by the National Natural Science Foundation of China under Contract (52176022, 51776145).

References

- [1] Levin LA, Bett BJ, Gates AR, Heimbach P, Howe BM, Janssen F. Global observing needs in the deep ocean. *Front Mar Sci* 2019;6:241. <https://doi.org/10.3389/fmars.2019.00241>.
- [2] Wang Y, Liu X, Chen T, Wang H, Zhu C, Yu H, et al. An underwater flag-like triboelectric nanogenerator for harvesting ocean current energy under extremely low velocity condition. *Nano Energy* 2021;90:106503. <https://doi.org/10.1016/j.nanoen.2021.106503>.
- [3] Bueno-Pardo J, Ramalho SP, García-Alegre A, Morgado M, Vieira RP, Cunha MR, et al. Deep-sea crustacean trawling fisheries in Portugal: quantification of effort and assessment of landings per unit effort using a Vessel Monitoring System (VMS). *Sci Rep* 2017;7:40795. <https://doi.org/10.1038/srep40795>.
- [4] Yu J, Zhang S, Yang W, Xin Y, Gao H. Design and application of buoy single point mooring system with electro-optical-mechanical (EOM) cable. *JMSE* 2020;8:672. <https://doi.org/10.3390/jmse8090672>.
- [5] Sloyan BM, Wanninkhof R, Kramp M, Johnson GC, Talley LD, Tanhua T, et al. The Global Ocean Ship-based hydrographic investigations Program (GO-SHIP): a

- platform for integrated multidisciplinary ocean science. *Front Mar Sci* 2019;6:445. <https://doi.org/10.3389/fmars.2019.00445>.
- [6] Barnes CR, Best MMR, Johnson FR, Pautet L, Pirenne B. Challenges, benefits, and opportunities in installing and operating cabled ocean observatories: perspectives from NEPTUNE Canada. *IEEE J Oceanic Eng* 2013;38:144–57. <https://doi.org/10.1109/JOE.2012.2212751>.
- [7] Zhang DY, Guo PH, Hu Q, Li JY. Parametric study and Multi-Objective optimization of a ductless Archimedes screw hydrokinetic Turbine: experimental and numerical investigation. *Energy Convers Manag* 2022;273:116423. <https://doi.org/10.1016/j.enconman.2022.116423>.
- [8] Zhang DY, Guo PH, Xu B, Li JY. A deep-water in-situ power generation system based on chain-driven hydrokinetic turbine. *J Clean Prod* 2023;385:135774. <https://doi.org/10.1016/j.jclepro.2022.135774>.
- [9] Zhang D, Guo P, Cheng Y, Hu Q, Li J. Analysis of blockage correction methods for high-solidity hydrokinetic turbines: experimental and numerical investigations. *Ocean Eng* 2023;283:115185. <https://doi.org/10.1016/j.oceaneng.2023.115185>.
- [10] Bean TP, Greenwood N, Beckett R, Biermann L, Bignell JP, Brant JL, et al. A review of the tools used for marine monitoring in the UK: combining historic and contemporary methods with modeling and socioeconomics to fulfill legislative needs and scientific ambitions. *Front Mar Sci* 2017;4:263. <https://doi.org/10.3389/fmars.2017.00263>.
- [11] Jingshuo N. Notice on soliciting public voyage demand for “qingyan sea trial 1” test mother ship in greater bay area. <https://ioe.sigs.tsinghua.edu.cn/2022/0704/c4334a55624/page.htm>. [Accessed 27 November 2022].
- [12] Chen X, Yang Y, Cui Z, Shen J. Vibration fault diagnosis of wind turbines based on variational mode decomposition and energy entropy. *Energy* 2019;174:1100–9. <https://doi.org/10.1016/j.energy.2019.03.057>.
- [13] Melo Junior FEDA, De Moura EP, Costa Rocha PA, De Andrade CF. Unbalance evaluation of a scaled wind turbine under different rotational regimes via detrended fluctuation analysis of vibration signals combined with pattern recognition techniques. *Energy* 2019;171:556–65. <https://doi.org/10.1016/j.energy.2019.01.042>.
- [14] Moussa I, Khedher A. Real-time WTE using FLC implementation on FPGA board: theoretical and experimental studies. In: 2020 17th international multi-conference on systems, signals & devices (SSD), monastir, Tunisia: ieee; 2020. p. 428–33. <https://doi.org/10.1109/SSD49366.2020.9364249>.
- [15] Averous NR, Stienecker M, Kock S, Andrei C, Helmedag A, De Doncker RW, et al. Development of a 4 MW full-size wind-turbine test bench. *IEEE J Emerg Sel Topics Power Electron* 2017;5:600–9. <https://doi.org/10.1109/JESTPE.2017.2667399>.
- [16] Carranza O, Figueres E, Garcerá G, Gonzalez LG. Comparative study of speed estimators with highly noisy measurement signals for Wind Energy Generation Systems. *Appl Energy* 2011;88:805–13. <https://doi.org/10.1016/j.apenergy.2010.07.039>.
- [17] Weijie L, Minghui Y, Rui Z, Minghe J, Yun Z. Investigating instability of the wind turbine simulator with the conventional inertia emulation scheme. In: 2015 IEEE energy conversion congress and exposition (ECCE). Montreal, QC, Canada: IEEE; 2015. p. 983–9. <https://doi.org/10.1109/ECCE.2015.7309795>.
- [18] Yu-shan L, Bao-ming G, Da-qiang B. Wind turbine real-time simulation based on discrete space vector modulation direct torque control. *J Syst Simul* 2011;23: 2611–6.
- [19] Schechner K, Hackl CM. Scaling of the drive train dynamics of large-scale wind turbine systems for real-time emulation in small-scale laboratory setups. *IEEE Trans Ind Electron* 2019;66:6779–88. <https://doi.org/10.1109/TIE.2018.2879287>.
- [20] Fan S, Liu Z. Proposal of fully-coupled actuated disk model for wind turbine operation modeling in turbulent flow field due to complex topography. *Energy* 2023;284:128509. <https://doi.org/10.1016/j.energy.2023.128509>.
- [21] Silva PASF, Shinomiya LD, De Oliveira TF, Vaz JRP, Amarante Mesquita AL, Acp Brasil Junior. Analysis of cavitation for the optimized design of hydrokinetic turbines using BEM. *Appl Energy* 2017;185:1281–91. <https://doi.org/10.1016/j.apenergy.2016.02.098>.
- [22] Zhang D, Guo P, Wang Y, Hu Q, Li J. Performance analysis of a ductless Archimedes screw turbine array for deep-sea power supply. *Ocean Eng* 2023;288: 116113. <https://doi.org/10.1016/j.oceaneng.2023.116113>.
- [23] Qu T, Kagimoto T, Yamagata T. A subsurface countercurrent along the east coast of Luzon. *Deep Sea Res Oceanogr Res Pap* 1997;44:413–23. [https://doi.org/10.1016/S0967-0637\(96\)00121-5](https://doi.org/10.1016/S0967-0637(96)00121-5).
- [24] Hu D, Hu S, Wu L, Li L, Zhang L, Diao X, et al. Direct measurements of the Luzon undercurrent. *J Phys Oceanogr* 2013;43:1417–25. <https://doi.org/10.1175/JPO-D-12-0165.1>.